



# Mirau-type full-field optical coherence tomography with switchable partially spatially coherent illumination modes

TUAN-SHU HO,<sup>1,4</sup> MING-RUNG TSAI,<sup>1</sup> CHIH-WEI LU,<sup>1</sup> HUNG-SHENG CHANG,<sup>1</sup> AND SHENG-LUNG HUANG<sup>1,2,3,5</sup>

<sup>1</sup>Apollo Medical Optics, Ltd., Taipei 114, Taiwan

<sup>2</sup>Graduate Institute of Photonics and Optoelectronics, National Taiwan University, Taipei 106, Taiwan

<sup>3</sup>Department of Electrical Engineering, National Taiwan University, Taipei 106, Taiwan

<sup>4</sup>Correspondence regarding OCT system design questions should be sent to [tuanshu@mdamo.com](mailto:tuanshu@mdamo.com)

<sup>5</sup>Correspondence regarding light source questions should be sent to [shaung@ntu.edu.tw](mailto:shaung@ntu.edu.tw)

**Abstract:** A crystalline-fiber-based Mirau-type full-field optical coherence tomography (FF-OCT) system utilizing two partially coherent illumination modes is presented. Using a diode-pumped Ti:sapphire crystalline fiber with a high numerical aperture, spatially-incoherent broadband emission can be generated with high radiance. With two modes of different spatial coherence settings, either deeper penetration depth or higher B-scan rate can be achieved. In a wide-field illumination mode, the system functions like FF-OCT with partially coherent illumination to improve the penetration depth. In a strip-field illumination mode, a compressed field is generated on the sample, and a low-speckle B-scan can be acquired by compounding pixel lines within.

© 2021 Optical Society of America under the terms of the [OSA Open Access Publishing Agreement](#)

## 1. Introduction

With broadband light sources and high-NA optics, optical coherence tomography (OCT) can provide cellular-resolution morphological images. Methods to extend the depth of focus [1] and recover out-of-focus resolution [2] were proposed, but generally, sensitivity drops as measurement depth are away from the focus. Fusing images with various focal settings can help to improve the overall sensitivity in an extended depth range [3,4]. For a system to operate near 1- $\mu\text{m}$  lateral resolution, the depth of focus is less than 10  $\mu\text{m}$ , and a huge number of acquisitions is necessary to reconstruct a single B-scan. To release the scanning burden, systems utilizing wide-field illumination and parallel detection in the transversal plane [5–7] were developed. However, for imaging within turbid tissue, a larger amount of crosstalk photon is collected by the detector, and the image quality is affected by coherent artifacts [6]. Methods like integrating high-speed deformable membrane for random phase modulation [8], using coherent laser and high-NA objective for line-field confocal gating [9] were proposed to suppress coherent crosstalk.

It is known that a spatially incoherent light source helps to reject crosstalk under a parallel detection scheme [10]. Broadband spatially incoherent source can be generated by coupling high-radiance light into a long multimode fiber [11], or use a halogen lamp [12], light-emitting diode [13] or laser-based fluorescence [14] as the light source. With spatially low-coherence illumination, the interference of crosstalk photons outside of the spatial coherence area is prevented. With a two-dimensional image sensor as the detector, OCT is often designed with full-field detection and coined as full-field OCT (FF-OCT). With a time-domain parallel detection scheme, millions of A-scans can be acquired within a single axial scan. Hence, due to the high *en face* rate, high-resolution volumetric images can be acquired at high speed even with a mechanical depth scan. The cost and complexity of spatially-incoherent broadband sources

are also much lower comparing to broadband lasers, which are required in ultrahigh-resolution point-scan or line-scan OCT systems [9].

There are two major problems that limit the *in vivo* applications of FF-OCT. The first issue is the acquisition time for a single B-scan is too long for most clinical applications. For example, FF-OCT that able to acquire *en face* images at  $> 10$  Hz rate, may require more than 5 seconds to reconstruct a single B-scan image with similar resolution. Another problem is the shallow penetration depth. In an FF-OCT system with a large-etendue light source, the coherence volume is less than or equal to the focal volume. For imaging within inhomogeneous turbid media, a large portion of photons may fall outside the coherence volume, either due to defocus or multiple scattering, and sensitivity reducing fast with depth [15,16]. It is possible to lengthen the penetration depth by performing spatial filtering [16]. However, it is difficult to apply in practice due to the insufficient radiance of conventional broadband sources, especially for *in vivo* applications that require high scan speed.

By drawing Ti:sapphire crystal into fiber form, inserted into glass capillary, and pumping with diode lasers, high-radiance broadband light can be generated [17]. In this report, we present a Mirau-type FF-OCT based on this high-radiance crystalline fiber source. The Mirau-type interferometer is advantageous for *in vivo* OCT applications because of its compactness, low-weight, and higher resistance to vibration. However, since the size of the reference mirror is at least equal to the field of view, the center of the light path is blocked in the FF-OCT system. This center obscuration results in optical loss and potentially reduces the lateral resolution. For wide-field OCT, especially FF-OCT, it may also cause illumination nonuniformity and stray light. Mirau-type wide-field OCT was proposed with some tweaks to partially solve the obscuration issue, for example, low-reflective reference mirror [18] or line-shaped reference mirror [19]. However, the former introduces huge optical loss to the system, while the latter cannot perform *en face* scanning. In this report, the obscuration problem of Mirau interferometry is avoided with a small-etendue light source and an off-axis illumination design while maintaining high optical throughput and the capability to perform wide-field imaging. Since the etendue of the crystal fiber is much smaller than the detection etendue of the FF-OCT system, it is operated under a partially spatially coherence illumination scheme, and the penetration depth within turbid media is increased. To suppress the crosstalk artifacts and increase the B-scan rate, a switchable lens design is utilized to adjust both the spatial coherence and field of illumination. A strip-shaped field of a 20- $\mu\text{m}$  width can be generated on the sample with high radiance and a comparably low spatial coherence. By compounding multiple pixel lines within the field, low-crosstalk B-scan with reduced speckle contrast can be acquired at a much higher rate.

## 2. Methodology

Dynamic focusing is usually required for FF-OCT and related techniques since it is important to align the focal plane and interference plane to ensure resolution and sensitivity. This can be achieved by either control two axes separately (each for focal and interference plane) or translate the whole interferometer during scanning [15]. The former raises the complexity and cost of the system, while the latter requires a high precision stage with a larger loading capacity. A low-weight interferometer like the Mirau design is thus preferred.

Ti:sapphire crystal is a popular laser medium for broadband light generation. With the laser-heated pedestal growth (LHPG) method, Ti:sapphire crystal can be drawn into fiber form with a core size down to 17 $\mu\text{m}$  while maintaining a higher doping concentration. With the fiber structure, both the pumping laser and fluorescence light is confined in a small region, and the output radiance significantly increased due to reduced etendue. By cladding the crystalline fiber with a glass capillary, the transmission loss can be reduced while maintaining a numerical aperture close to 1 to capture the most of fluorescent photon. The number of supported modes of the crystal fiber is determined by both crystalline core size and refractive index difference between

core and cladding. With the described parameter, the V-number is around 60, and the estimated number of modes is around 2000. The corresponding radiance is around  $50 \text{ W} \cdot \text{sr}^{-1} \cdot \text{mm}^{-2}$ , which roughly is 10~1000 times larger than conventional spatially-incoherent light sources (halogen lamps, light emitting diodes) at similar bandwidth. The details of diode-laser pumped crystalline fiber light sources used in our FF-OCT system are provided in [17]. The fluorescence light is coupled into a long small-core multimode fiber (FG105LCA, 10 m) to ensure there is no residual coherence and for ease to applications. The output power and optical etendue is 30 mW and  $1400 \mu\text{m}^2 \cdot \text{sr}$ , respectively. Since the optical etendue of this source is at least two orders smaller than the detection etendue of typical FF-OCT, a coherence volume larger than the focal volume can be achieved without severe spatial filtering.

The method we used to adopt a small etendue light source to full-field Mirau interferometry is shown in Fig. 1. For simplicity, the pupil plane is set to the back focal plane of the objective lens. Three glass plates are set between the objective lens and the sample, which are the reference plate, beamsplitter, and probe window, respectively. The central region of the reference plate is metal-coated and highly reflective ( $R > 95\%$ ), while the peripheral region is transparent. To sustain full-field imaging, the size of the reference mirror must be at least the size of the field of view. From the sample's point-of-view, this reference mirror projects a shadow to the pupil plane and obscures the central light path. From the source's point-of-view, the fiber tip shall be imaged at the pupil plane of the objective lens for wide-field illumination. With the optical invariant, the angular aperture of illumination can be estimated as  $\Phi_{MMF} NA_{MMF} / \Phi_{FOI}$ , where  $\Phi_{MMF}$  and  $NA_{MMF}$  is the size and numerical aperture of the multimode fiber, and  $\Phi_{FOI}$  is the size of the illumination field. With the described high-radiance crystal fiber light source, the illumination NA is less than 0.05 when the size of the field of illumination (FOI) is around 1 mm. Since this is much smaller than the typical NA for FF-OCT with  $\sim 1\text{-}\mu\text{m}$  resolution, only a small portion of the objective aperture is required for illuminating light to pass through. Therefore, by imaging of fiber tip to the pupil plane of imaging optics and ensuring the chief ray is parallel to the optical axis with a small offset, a uniform field of illumination can be generated on the sample plane without being obscured.

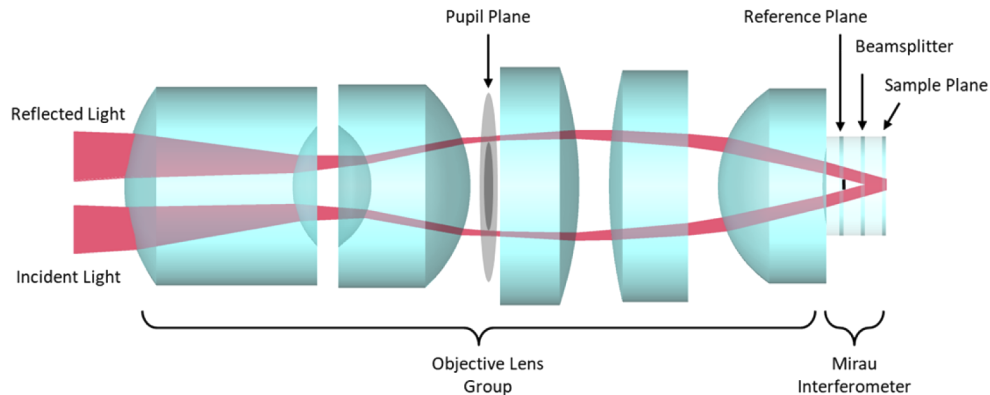


**Fig. 1.** Schematic diagram of the illumination pathway (incident and reflected) in Mirau objective lens. The reference beam is not shown for image clarity.

An objective lens is customized to correct the chromatic dispersion caused by the Mirau structure. Resolution is optimized for an immersed object space with described glass plates in the near-infrared wavelength range (650~950 nm). The refractive index of the immersion liquid is chosen to be close to human skin ( $\sim 1.4$ ) to avoid aberration during dynamic focusing. The chamber between the reference plate and beamsplitter is also filled with a medium of a refractive index similar to the immersion liquid, so the optical path length of the sample arm and reference

arm is roughly the same. Since the reference mirror is away from the sample plane, the area obscuration ratio by the reference mirror is about 5%. The beam splitting ratio is 1:4, and more than 70% of photons backscattered from the sample can be collected by the objective lens.

The schematic diagram of the Mirau-type FF-OCT system is shown in Fig. 2(a). A typical polarization beamsplitter and quarter waveplate geometry are used to circulate the light between illumination optics, Mirau objective lens, and a two-dimensional camera. Since the etendue of the light source is much smaller than the detection etendue of imaging optics, there are some degrees of freedom to adjust the size of FOI while maintaining throughput. The light emitted from the fiber is firstly collimated and then directed to a motorized turret. By changing field lenses of different dioptric power, the light spot on the pupil plane and size of FOI changes accordingly. A design with a pick-off wedge plate is used to improve the spatial uniformity and angular symmetry of the illumination field. The light after the field lens optics is partially refracted by the wedge plate and then separated into two sub-beams. By adjusting the angle of the whole illuminating module, the chief ray of each sub-beam can be set to parallel to the optical axis of the imaging system. As a result, two light spots are projected to the pupil plane symmetrically and are both away from the obscured center. With the pick-off wedge plate, the high-intensity rays are directed to the peripheral region of the field of view. The corresponding FOIs overlapped with each other on the sample plane symmetrically. Two examples of different field lenses are shown in Fig. 2(b). With a spherical field lens, the tip of multimode fiber is reimaged at the pupil plane as two small spots, and the sample plane is uniformly illuminated from two directions within  $0.5 \times 0.5 \text{ mm}^2$ . The other example with a cylindrical field lens is shown in Fig. 2(c). With the power axis orthogonal to the edge wedged plate, two elliptical spots are projected to the pupil plane, and a strip illumination field of line width  $\sim 20 \mu\text{m}$  is generated on the sample. With a much small size of FOI, the intensity is significantly higher than the case of wide-field illumination.

In the wide-field illumination mode, the system is quite similar to the conventional FF-OCT system, and volumetric imaging can be achieved by translating the Mirau objective lens relative to the sample and continuous recording the interferogram projected on the camera. In the strip-illumination mode, a narrow FOI is generated on the sample and projected to the camera plane. With light tensely focused on the sample, the B-scan scanning rate can be improved with a shorter required exposure time. This mode is useful for the clinical condition that requires rapid examination along the cross-sectional direction. For example, to reveal the microstructure near the dermal-epidermal junction of human skin. It shall be noted that the size of spatial coherence volume is much different in the two described illumination modes. Since the output of the multimode fiber is spatially incoherent, the spatial coherence area on the sample plane is inversely proportional to the spot size on the pupil plane. In the wide-field illumination mode, the images of multimode fiber tips on the pupil plane are small, and the corresponding coherence volume is much larger than the focal volume of the imaging optics. Therefore, although interference of many multiple-scattered photons is prevented, some interference outside of focal volume is still permitted. As mentioned in the previous section, the refractive index of human tissue is inhomogeneous. For example, the average refractive index of human skin is dependent on depth and tissue type [20]. The mismatch between the average refractive index between bio-tissue and immersion liquid leads to the small displacement between focal and interference plane within the sample tissue. With a larger coherence volume, some displacement between the focal and interference plane is allowed, and the overall penetration depth on various tissue types can be improved. On the other hand, the spatial coherence volume is much smaller in the strip-field illumination mode. More precisely, the spatial coherence radius along the axis that light being tensely focused is extremely short. This improves the sectioning capability by rejecting coherent crosstalk from adjacent B-scan planes.



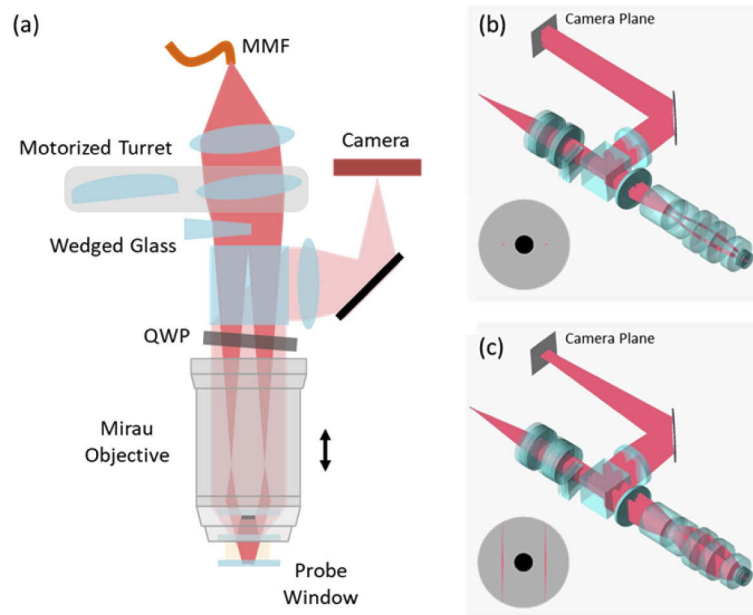


**Fig. 2.** Off-axis illumination for Mirau-type FF-OCT. Schematic diagram of (a) System. MMF: multimode fiber. QWP: quarter waveplate. (b) Simulated three-dimensional ray diagram for wide-field illumination mode. (c) strip-field illumination mode. The insets in (b) and (c) show the aperture diagram at the aperture plane of the objective lens. Central black spot: region being obscured by reference mirror. Red light spots: illuminating light spots.

The image quality of OCT is impacted by speckle [21]. The speckle noise in OCT is multiplicative and appears as a grainy pattern overlap on the sample structure. The speckle pattern can be misleading and make small organelles like nuclei and clusters of melanin difficult to be identified. The speckle can be mitigated by averaging images with low correlation. Despeckle methods like temporal compounding [22], spatial compounding [23,24] and other techniques can be found in the literature. Temporal compounding can be achieved by simply averaging successive *en face* images or B-scans, and does not require hardware modification. In order to suppress the speckle contrast with temporal averaging, the speckle pattern must be decorrelated over the time window of acquisition. For *in vivo* dermatologic applications, we found the micro-motions within a tissue is not always enough to decorrelate the speckle pattern even at the timescale of seconds, especially for B-scans. Although the speckle contrast can be somewhat reduced with a longer acquisition window, the images are more likely to be blurred due to sample movement, and the effective resolution is reduced.

In the strip-field illumination mode, strip-shaped FOI with around 20- $\mu\text{m}$  linewidth is generated on the sample plane. The linewidth is determined by the core size of multimode fiber and the magnification of the illuminating optics. To fulfill the Nyquist sampling requirement, an around 0.5- $\mu\text{m}$  sampling resolution is used in the imaging system. By setting the direction of the illumination field to be parallel to the camera pixel lines and activate multiple pixel lines within FOI during scanning, more than 30 B-scans can be acquired within one axial scan. We found that the image correlation between close adjacent B-scans is very low, and by compounding few adjacent B-scans with low correlation, the speckle contrast is significantly reduced. Comparing to temporal compounding, this spatial compounding approach does not rely on micro-movement of sample and does not require high-speed mechanical scanning. By stacking adjacent pixel lines for a single B-scan, the virtual slice thickness of the B-scan increased. For reference, a typical

thickness of the histologic slice is around  $5\ \mu\text{m}$ , equal to around 10 pixels in described FF-OCT system. To avoid blurring due to different sample structures within the finite thickness of the virtual slice, we decompose the B-scans into two-level Gaussian pyramids and treat the high and low-frequency images in different ways. The pyramid decomposition was reported to be helpful to retain subtle features during despeckling process [25]. The flowchart for the compounding process is shown in Fig. 3. The high-pass layer contains speckle and high-resolution details of the sample, while the low-pass layer contains structural information much larger than the grain size of the speckle. To reduce the speckle contrast, it is only necessary to perform spatial compounding the high-spatial frequency layer of the pyramid, and unnecessary blurriness can be avoided. After the image reconstruction process, the image with reduced speckle contrast and preserving structural details can be generated.

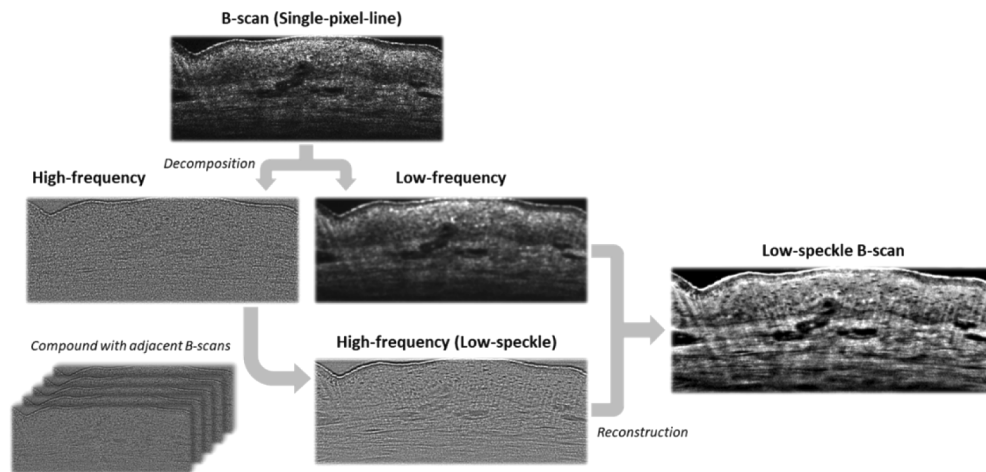


**Fig. 3.** Flowchart for spatial compounding procedure

### 3. Result and discussion

#### 3.1. Spatial resolution

The axial and lateral resolution measurement result is shown in Fig. 4. The axial resolution is determined by measuring the specular reflection of the probe window (fused silica glass). During scanning, the whole Mirau objective lens is translated relative to the sample along the depth direction, and the camera is continuously recording the interferogram. The full-width half maximum of the point spread function is around  $1.3\ \mu\text{m}$ , slightly higher than the previously reported value with the similar light source ( $1.1\ \mu\text{m}$ ), because of the low responsibility of camera using in the near-infrared region. No significant difference of axial resolution between the two modes (of different spatial coherence settings) was found in this measurement, suggesting the axial resolution is mostly defined by the temporal coherence.

The lateral resolution of the imaging system is estimated by measuring the line-spread function of a sharp edge. All measurements were done under the Mirau structure and with a reference mirror of a size larger than the field on view in the center of the light path. Since the FF-OCT system is designed near Nyquist sampling, and the measurement was done in a slant-edge measurement scheme to avoid sampling error [26]. A resolution target with 5-degree-slanted sharp edges (Thorlabs R2L2S2P) is used as the test sample. A MATLAB program based on sfrmat3 (an implementation of ISO 12233) was used to analyze the result. Super-resolved edge-spread function with  $\sim 0.13\ \mu\text{m}$  sampling resolution is reconstructed from every 100 pixels

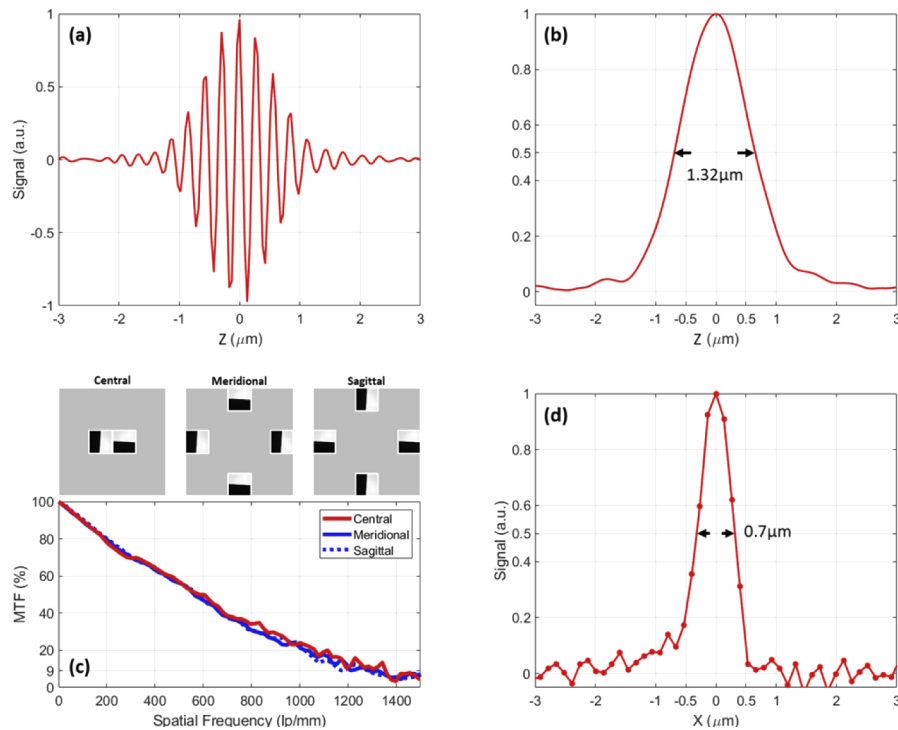


**Fig. 4.** The spatial resolution of the FF-OCT system. (a) Axial point spread function. (b) Demodulated axial point spread function. (c) Modulation transfer function measurement result. (d) Transversal line spread function at the center of the field.

$\times 100$  pixels image of slant edge. Both modulation transfer function (MTF) and line-spread function (LSF) can be derived from the result. The MTF at 5 different points in the  $550 \mu\text{m} \times 550 \mu\text{m}$  field-of-view along both horizontal and vertical directions were measured. The results are grouping into central, meridional, and sagittal, as shown in Fig. 4(c). The averaged MTF curves of the three groups are almost the same, and MTF at 1000 line pairs/mm is around 20%. For FF-OCT, the MTF is an essential indicator not only for resolution but also because it is related to the ratio of crosstalk photon and hence affecting the system sensitivity [11]. An LSF from the central group is shown in Fig. 4(d), and the full-width half maximum of the LSF is around  $0.7 \mu\text{m}$ .

To evaluate the image resolving capability, a commercial-available 1951 USAF resolution target is used as the test sample (Edmund #58-198) for both illumination modes. The finest pattern (645 line pairs/mm, Group 9 Element 3) on the target is corresponding to  $\sim 1.55\text{-}\mu\text{m}$  width of line pair and  $\sim 0.78\text{-}\mu\text{m}$  width of each black and white line. The full-frame OCT images under both illumination modes are shown in Figs. 5(a-b). The OCT images are generated with conventional 4-frame demodulation [27]. In the strip-illumination mode, only the pattern within the illumination band can be imaged. The 645-line pairs/mm pattern can be clearly imaged under both illumination modes. To evaluate the resolving power of the FF-OCT system within turbid bio-tissue, the OCT images of the resolution target behind the turbid layer were also measured. The Scotch tape (Scotch Magic Tape, 3M, USA) was used to mimic a turbid tissue. The tape is a highly-scattering layer of thickness around  $60 \mu\text{m}$  (roughly  $50 \mu\text{m}$  under pressure). Images with 1~2 layers of tape were measured under both illumination modes. With a narrow temporal coherent gate and spatially partially coherent illumination, a higher percentage of multiply

scattered photons can be rejected, and good lateral resolution can be preserved behind turbid media. As shown in Figs. 5(c-d), the 645-line pairs/mm pattern can be resolved behind tapes under both illumination modes. Under the strip illumination modes, where the spatial coherence area is smaller, the pattern is less distorted comparing to the wide-field illumination mode.

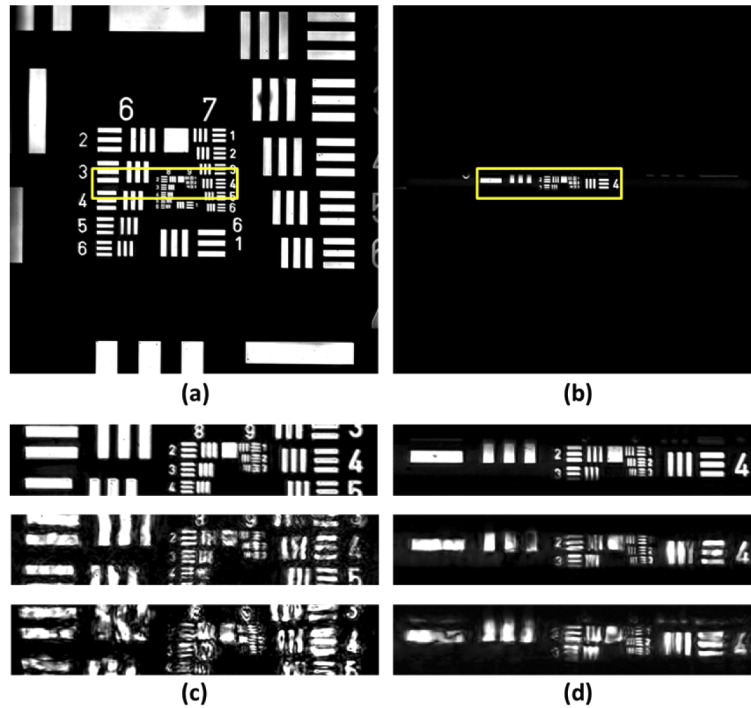


**Fig. 5.** FF-OCT images of 1951 USAF resolution target. (a) under wide-field illumination mode. The field of view is  $540 \times 540 \mu\text{m}$ . (b) under strip-field illumination mode. (c~d) Zoomed images for the central region for wide-field and strip-field illumination mode, respectively. The number of scotch tape layers in the light path from top to bottom: 0, 1, 2.

### 3.2. Penetration depth in turbid media

The OCT signal profile versus depth was measured on a turbid phantom. The phantom is formed by a roll of Scotch tape. The tapes (refractive index  $\sim 1.47$ ) are immersed in silicone oil (refractive index  $\sim 1.4$ ), and scattering due to the refractive index fluctuation is collected by FF-OCT. With the high-radiance crystalline fiber source with small etendue, the light can be coupled into the multimode fiber of small core size ( $106 \mu\text{m}$ ) and low NA (0.22) without a significant loss (roughly 20% coupling loss). With the small-etendue multimode fiber, the spatial coherence area of FF-OCT is large, and imaging depth increases. To compare the imaging depth under different spatial coherence settings, OCT B-scan images of the same phantom were measured with different multimode fibers. Other than the multimode fiber used in our system (FG105LCA), large-core multimode fibers (FT400EMT, FT1000EMT) are typically used for high-brightness light-emitting diodes coupling were tested for comparison. The core size/fiber NA are  $400 \mu\text{m}/0.39$  and  $1000 \mu\text{m}/0.39$ , respectively. The etendue is roughly  $62522 \mu\text{m}^2 \cdot \text{sr}$  and  $390763 \mu\text{m}^2 \cdot \text{sr}$ , respectively, and are roughly 44 and 278 times larger than FG105LCA. It shall be noted that the etendue of the large-core multimode fiber is still much smaller than the most conventional halogen lamps.

The OCT B-scan images of the same turbid phantom measured with different MM fibers are shown in Figs. 6(a-c). The system configuration other than the MM fibers is the same for all measurements. The exposure time of the camera was adjusted to make the pixels operated under a similar saturation level. With the high-radiance light source, the exposure time required for the camera to hit saturation is similar for all fibers (less than 20% difference). It also is confirmed that the light that arrives on the camera plane is mostly backscattered/reflected light from the sample/reference plane (in other words, no significant stray light problem) in all measurements. The B-scan images are reconstructed with conventional Hilbert transform for time-domain OCT [28]. The B-scan images shown here are based on the same brightness/contrast setting (linear-scaled). The overall signal with multimode fibers of smaller etendue is obviously higher. The signal profiles versus depth of different multimode fibers are shown in Fig. 6(d). The signal is defined as the difference between the OCT signal and the incoherent background. The signal plot is normalized and log-scaled. With the MMF1 (FG105LCA), the signal to noise ratio of the very first Scotch tape layer is roughly 50 dB. At the deepest region in the scan range ( $\sim 400$   $\mu\text{m}$  depth), there is roughly a 25-dB difference of signal between setting with MMF1 and MMF3 (FT1000EMT). As expected, the signal drops much slower with the small-etendue multimode fiber since the spatial coherence volume is larger, and more interference signal from multiple-scattered and out-of-focus photons is preserved. Experiments have also been performed on bio-tissue, and similar results were yielded on various types of skin tissues. Some *in vivo* B-scan images with prolonged penetration on human skin will be presented in the next section.

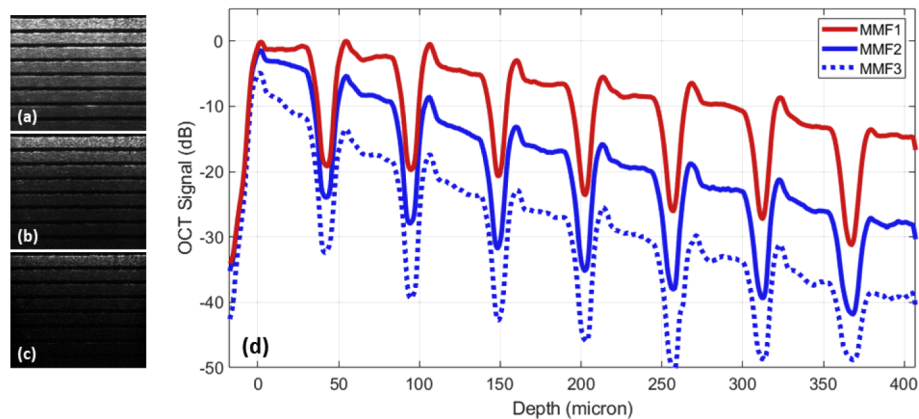


**Fig. 6.** B-scans of a roll of scotch tape. (a~c) with FG105LCA (MMF1), FT400EMT (MMF2), and FT1000EMT (MMF3), respectively. (d) Signal profile versus depth.

### 3.3. *In vivo* FF-OCT under wide-field illumination mode

The full well capacity and responsibility in the near-infrared region of the camera (PhotonFocus MV1-D1024E) used is approximately 200k electrons and 140k electrons/lux-s, respectively. With the high-radiance Ti:sapphire crystal fiber light source, the exposure time required to hit saturation by the reference beam in the described FF-OCT system is short ( $< 1$  ms), the camera can be operated at 120-Hz full-frame frame rate, and the corresponding *en face* imaging rate is 30 Hz. By translating the objective lens forward and backward in a small depth range, this mode can also be used to perform continuous *en face* imaging at a similar depth, providing a quick examination of the morphological structure beneath the superficial surface and for physicians to locate the region of interest. A set of FF-OCT images is presented in Fig. 7. Cellular features like the shape of nuclei of keratinocyte, cluster of melanin, and boundary of the dermal-epidermal junction can be clearly imaged. Another example of a volumetric image near a red-stained lesion



is shown in Fig. 8. A build-in dermoscope (sharing the same objective lens with FF-OCT) is used to assist in locating the lesion, as shown in the inset of Fig. 8(a), and a serial of FF-OCT images is captured at different depth. A hyporeflective region with a worm-shaped structure was identified beneath the dermal-epidermal junction by FF-OCT, and the densities of nuclei of keratinocytes obviously increased near the lesion. Under wide-field illumination mode, the described system can penetrate bio-tissues much deeper compared to a previous publication [18] due to both longer wavelength and larger spatial coherence area. Some B-scan images reconstructed from *en face* images acquired under wide-field illumination mode are shown in Fig. 9. With deeper penetration on human skin, the system is able to reveal the arrangement of collagen fibers and microvascular structure, and other organelles in the upper dermis.

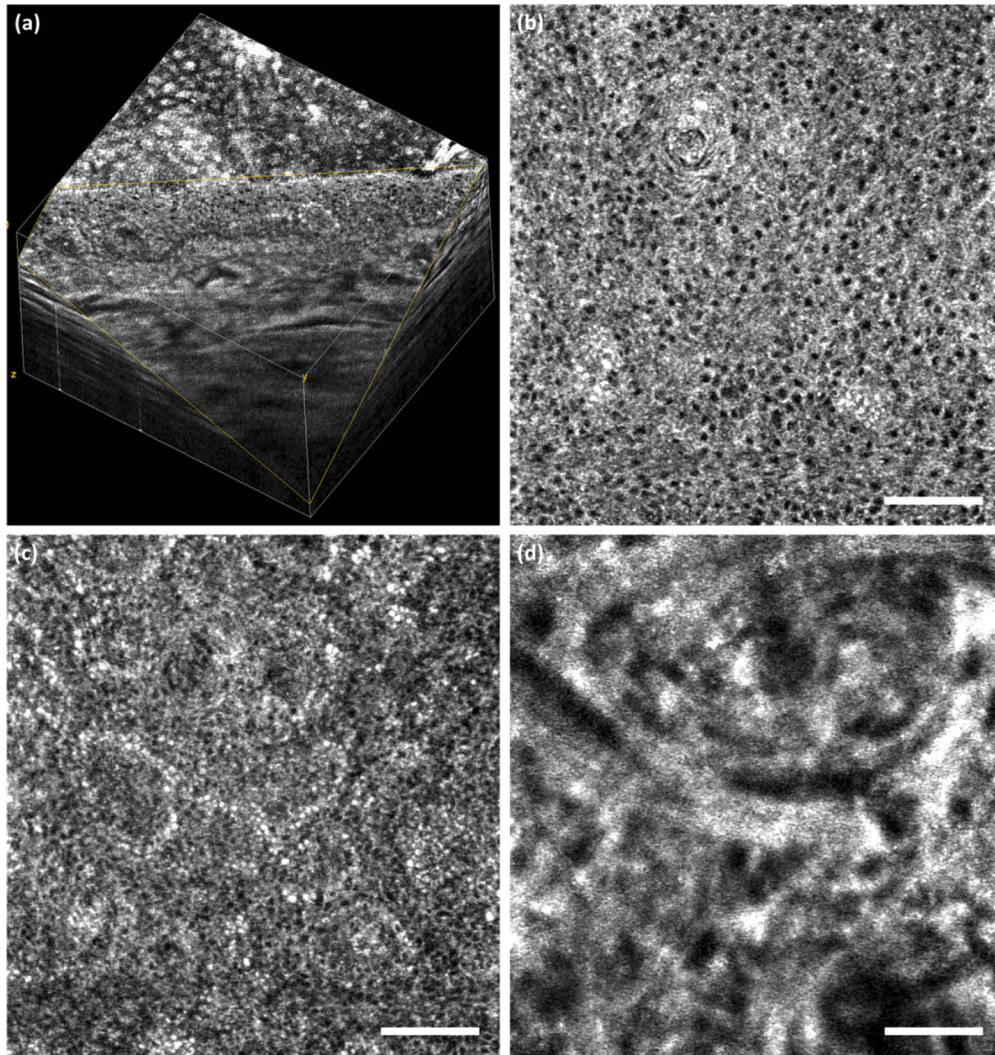


**Fig. 7.** *In vivo* FF-OCT images acquired under wide-field illumination mode on a Type 3 skin. (a) Three-dimensional-rendered volumetric image with one corner cut to visualize cross-sectional view. The three-dimensional image stack was acquired within 43 seconds. (b) *En face* image acquired at the upper dermis (stratum granulosum/spinosum). (c) near melanin cap and upper rete ridge. (d) in the upper dermis. The scale bar represents 100µm. 3D-rendered images are produced with *Volume Viewer* in *Fiji – ImageJ*.

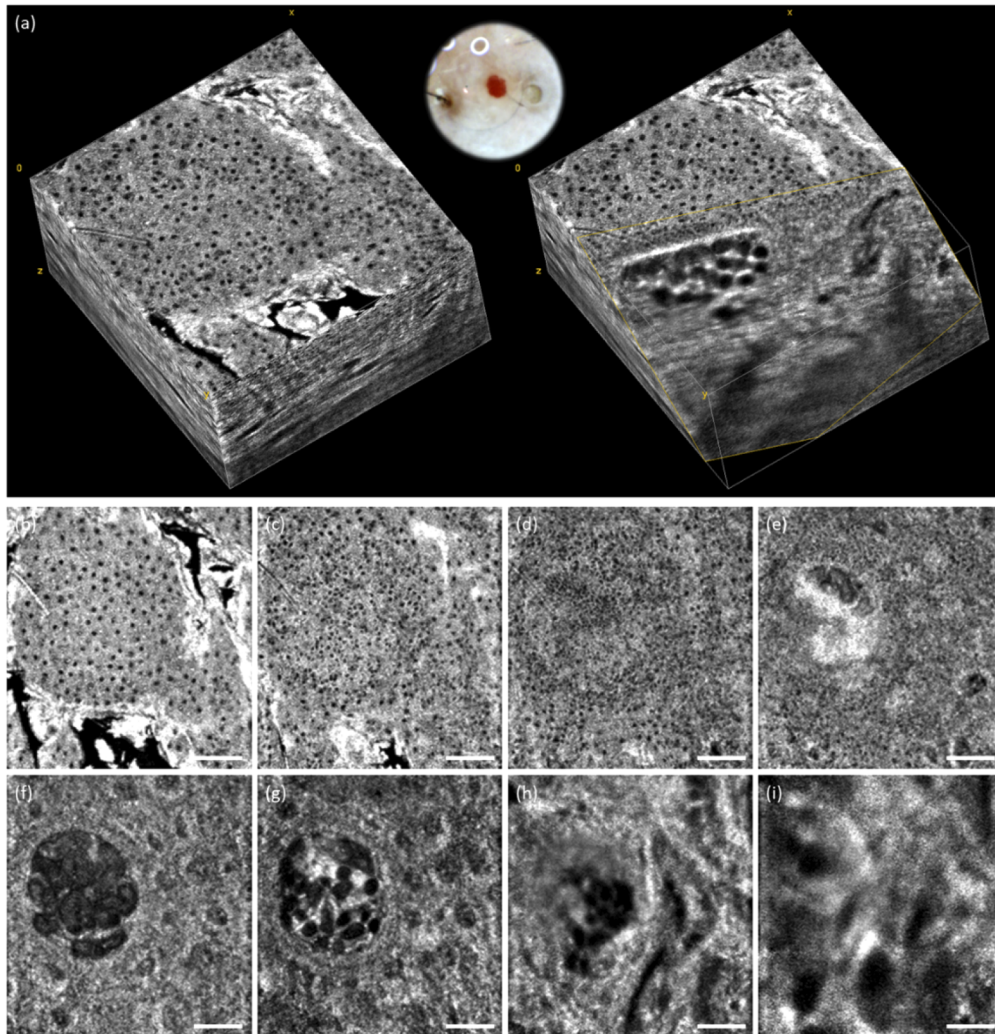


**Fig. 8.** *In vivo* FF-OCT images acquired near a red lesion. (a) Three-dimensional-rendered image stacks of the same site. One corner of the stack to the right is cut to visualize the cross-sectional view. Inset: dermoscopic image acquired by a built-in color camera. (b-i) *en face* images in the same image stack, different depth. The scale bar represents 100  $\mu\text{m}$ .

### 3.4. B-scan under strip-field illumination mode

The motor turret and the region of interest of the two-dimensional camera are both controlled by a computer. The turret is designed with high position repeatability, and the FF-OCT system can be switched between two modes instantly by clicking a button. Under the strip-field illumination mode, the required exposure time for the camera to saturate is about 20~30 times lower than the case of wide-field illumination. Besides, the spatial coherence of illumination light is significantly reduced, and more crosstalk photons are rejected by spatial coherence gating. By activating a single line of the two-dimensional camera, the maximum camera frame rate is around 40 kHz, and the corresponding acquisition time for a B-scan across 400  $\mu\text{m}$  depth is about 140 ms. However, the B-scan image acquired with a single-pixel line is seriously corrupted by speckle, and cellular detail is buried under speckle pattern. To suppress the speckle noise, multiple pixel



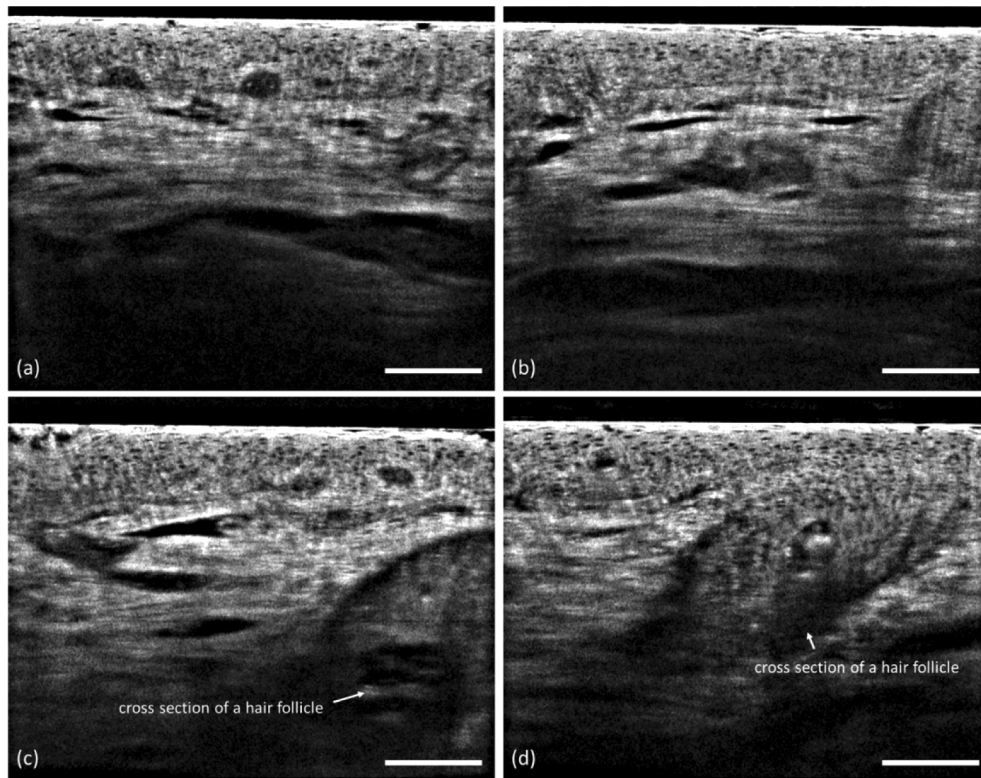


**Fig. 9.** FF-OCT B-scan images under wide-field illumination mode. The acquisition time for each image was within 4.5 seconds. (a-d) acquired on mid-cheek of a healthy volunteer of Fitzpatrick skin type 3. (c-d) near hair follicles. The image size is  $500 \times 400 \mu\text{m}$ , and the scale bar represents  $100\mu\text{m}$ .

lines ( $> 3$ -pixel lines) are activated during the B-scan mode, and the maximum camera frame rate is around 25 kHz, and the corresponding acquisition time for a  $400\text{-}\mu\text{m}$ -depth B-scan is around 250 ms. By compounding adjacent 3-pixel lines, the speckle pattern of the B-scan is significantly mitigated, and signal to noise (white Gaussian noise) ratio is typically higher than 30 dB in the epidermis and dermal-epidermal junction on Type 3 skin. Image details, like the shapes and orientations of nuclei of keratinocyte, the boundary of dermal-epidermal junction, and collagen arrangement in the papillary dermis, can be more clearly visible. An example is shown in Fig. 10.

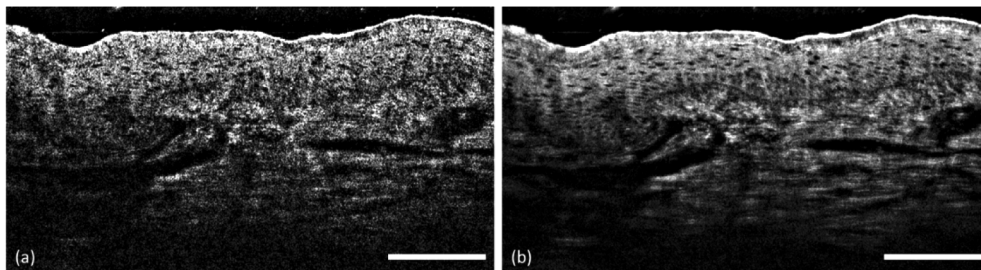


**Fig. 10.** *In vivo* B-scan images measured on human skin with different virtual slice thicknesses. (a)  $0.5 \mu\text{m}$  and (b)  $5 \mu\text{m}$ . The scale bar represents  $100 \mu\text{m}$ .

The number of activated pixel lines and corresponding virtual slice thickness can be adjusted without hardware modification (at a maximum thickness of 20  $\mu\text{m}$ ). With slice thickness larger than 5  $\mu\text{m}$ , the described pyramid decomposition can be applied to avoid unwanted blurriness. Typically, a Gaussian filter with  $\sigma$  between 1~3 pixels was used to generate the pyramid for better visualization of cellular details. Some more B-scan images are shown in Fig. 11. The distribution of nuclei in the epidermis, melanin near the dermal-epidermal-junction, and collagen fibers in the upper dermis can be clearly visualized.

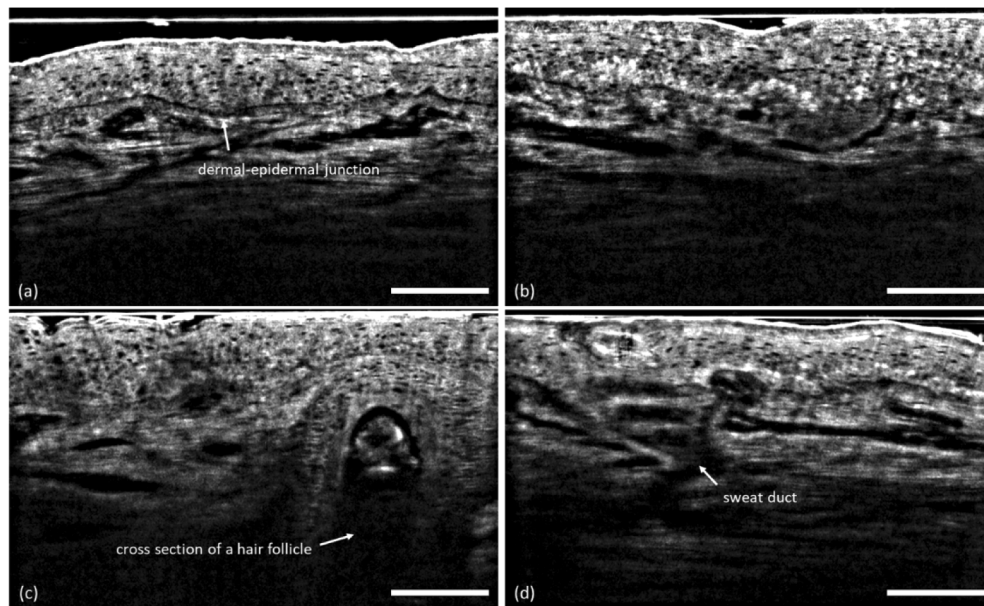


**Fig. 11.** *In vivo* B-scan images measured on various sites on human skin. The acquisition time for each image was 430 milliseconds. (a) volar forearm, (b) nevus, (c) near a hair follicle, and (d) near a sweat duct. The scale bar represents 100  $\mu\text{m}$ .

#### 4. Conclusion

In summary, a Mirau-type FF-OCT based on Ti:sapphire crystalline fiber light source is presented. By incorporating two different partially coherence illumination modes in one system, the advantages of using the high-radiance of crystalline fiber source in FF-OCT, including increased penetration depth and B-scan rate, are demonstrated. With a wide-field illumination mode of larger spatial coherence area, the system is able to provide volumetric images up to 400  $\mu\text{m}$  depth in turbid tissue, which usually cover the upper region of the reticular dermis of human skin. With a motorized turret to exchange the illumination field lens, the system is able to switch to a strip-illumination mode. With the tensely-focused illumination field by the high-radiance source, the camera frame rate can be run 8~40 times faster, depending on the number of pixel lines being activated, and B-scan acquisition time less than 0.5 seconds can be easily achieved. By activating multiple pixel lines within the strip illumination field of finite width, multiple B-scans can be simultaneously acquired. This provides a reliable way to suppress the speckle noise through spatial compounding, and B-scan with an appearance closer to histologic slices can be obtained by setting virtual slice thickness to typical slice thickness. With the switchable scheme between the *en face* and cross-section images, the FF-OCT could offer physicians and clinicians a flexible view on the lesion for facilitating early disease diagnosis.

**Disclosures.** The authors declare that there are no conflicts of interest related to this article.

## References

1. C. Blatter, B. Grajciar, C. M. Eigenwillig, W. Wieser, B. R. Biedermann, R. Huber, and R. A. Leitgeb, "Extended focus high-speed swept source OCT with self-reconstructive illumination," *Opt. Express* **19**(13), 12141 (2011).
2. A. Grebenyuk, A. Federici, V. Ryabukho, and A. Dubois, "Numerically focused full-field swept-source optical coherence microscopy with low spatial coherence illumination," *Appl. Opt.* **53**(8), 1697 (2014).
3. J. Holmes and S. Hattersley, "Image blending and speckle noise reduction in multi-beam OCT," in J. G. Fujimoto, J. A. Izatt, and V. V. Tuchin, eds. (2009), p. 71681N.
4. J. P. Rolland, P. Meemon, S. Murali, K. P. Thompson, and K. Lee, "Gabor-based fusion technique for Optical Coherence Microscopy," *Opt. Express* **18**(4), 3632 (2010).
5. T. Bonin, G. Franke, M. Hagen-Eggert, P. Koch, and G. Hüttmann, "In vivo Fourier-domain full-field OCT of the human retina with 15 million A-lines/s," *Opt. Lett.* **35**(20), 3432 (2010).
6. B. Grajciar, M. Pircher, A. F. Fercher, and R. A. Leitgeb, "Parallel Fourier domain optical coherence tomography for in vivo measurement of the human eye," *Opt. Express* **13**(4), 1131 (2005).
7. B. Huang, P. Bu, X. Wang, N. Nan, and X. Guo, "Speckle reduction in parallel optical coherence tomography by spatial compounding," *Opt. Laser Technol.* **45**, 69–73 (2013).
8. P. Stremplewski, E. Aukorius, P. Wnuk, Ł. Kozioł, P. Garstecki, and M. Wojtkowski, "In vivo volumetric imaging by crosstalk-free full-field OCT," *Optica* **6**(5), 608 (2019).
9. A. Dubois, O. Levecq, H. Azimani, A. Davis, J. Ogien, D. Siret, and A. Barut, "Line-field confocal time-domain optical coherence tomography with dynamic focusing," *Opt. Express* **26**(26), 33534 (2018).
10. B. Karamata, P. Lambelet, M. Laubscher, R. P. Salathé, and T. Lasser, "Spatially incoherent illumination as a mechanism for cross-talk suppression in wide-field optical coherence tomography," *Opt. Lett.* **29**(7), 736 (2004).
11. A.-H. Dhalla, J. V. Migacz, and J. A. Izatt, "Crosstalk rejection in parallel optical coherence tomography using spatially incoherent illumination with partially coherent sources," *Opt. Lett.* **35**(13), 2305 (2010).
12. L. Vabre, A. Dubois, and A. C. Boccara, "Thermal-light full-field optical coherence tomography," *Opt. Lett.* **27**(7), 530 (2002).
13. E. Beaurepaire, A. C. Boccara, M. Lebec, L. Blanchot, and H. Saint-Jalmes, "Full-field optical coherence microscopy," *Opt. Lett.* **23**(4), 244 (1998).
14. D. Sacchet, M. Brzezinski, J. Moreau, P. Georges, and A. Dubois, "Motion artifact suppression in full-field optical coherence tomography," *Appl. Opt.* **49**(9), 1480 (2010).
15. A. Dubois, "Focus defect and dispersion mismatch in full-field optical coherence microscopy," *Appl. Opt.* **56**(9), D142 (2017).
16. D. L. Marks, B. J. Davis, S. A. Boppart, and P. S. Carney, "Partially coherent illumination in full-field interferometric synthetic aperture microscopy," *J. Opt. Soc. Am. A* **26**(2), 376 (2009).
17. S.-C. Wang, T.-I. Yang, D.-Y. Jheng, C.-Y. Hsu, T.-T. Yang, T.-S. Ho, and S.-L. Huang, "Broadband and high-brightness light source: glass-clad Ti:sapphire crystal fiber," *Opt. Lett.* **40**(23), 5594 (2015).
18. C.-C. Tsai, C.-K. Chang, K.-Y. Hsu, T.-S. Ho, M.-Y. Lin, J.-W. Tjiu, and S.-L. Huang, "Full-depth epidermis tomography using a Mirau-based full-field optical coherence tomography," *Biomed. Opt. Express* **5**(9), 3001 (2014).
19. A. Dubois, W. Xue, O. Levecq, P. Bulkin, A.-L. Coutrot, and J. Ogien, "Mirau-based line-field confocal optical coherence tomography," *Opt. Express* **28**(6), 7918 (2020).
20. H. Ding, J. Q. Lu, W. A. Wooden, P. J. Kragel, and X.-H. Hu, "Refractive indices of human skin tissues at eight wavelengths and estimated dispersion relations between 300 and 1600 nm," *Phys. Med. Biol.* **51**(6), 1479–1489 (2006).
21. J. M. Schmitt, S. H. Xiang, and K. M. Yung, "Speckle in optical coherence tomography," *J. Biomed. Opt.* **4**(1), 95–105 (1999).
22. A. Davis, O. Levecq, H. Azimani, D. Siret, and A. Dubois, "Simultaneous dual-band line-field confocal optical coherence tomography: application to skin imaging," *Biomed. Opt. Express* **10**(2), 694 (2019).
23. M. R. N. Avanaki, R. Cernat, P. J. Tadrous, T. Tatla, A. Gh. Podoleanu, and S. A. Hojatoleslami, "Spatial compounding algorithm for speckle reduction of dynamic focus OCT images," *IEEE Photonics Technol. Lett.* **25**(15), 1439–1442 (2013).
24. M. Szkulmowski, I. Gorczynska, D. Szlag, M. Sylwestrzak, A. Kowalczyk, and M. Wojtkowski, "Efficient reduction of speckle noise in Optical Coherence Tomography," *Opt. Express* **20**(2), 1337 (2012).
25. J. Park, J. Kang, J. H. Chang, and Y. Yoo, "Speckle reduction techniques in medical ultrasound imaging," *Biomed. Eng. Lett.* **4**(1), 32–40 (2014).
26. P. Burns, "Slanted-edge MTF for digital camera and scanner analysis," *Proc. IS&T 2000 PICS Conference*, 135–138 (2000).
27. K. G. Larkin, "Efficient nonlinear algorithm for envelope detection in white light interferometry," *J. Opt. Soc. Am. A* **13**(4), 832–843 (1996).
28. G. S. Kino and S. S. C. Chim, "Mirau correlation microscope," *Appl. Opt.* **29**(26), 3775 (1990).